Surface & Coatings Technology 451 (2022) 129035

Contents lists available at ScienceDirect

Surface & Coatings Technology

journal homepage: www.elsevier.com/locate/surfcoat

Smooth semicompact multilayer coating of TiO_2 obtained by combining anodic oxidation and sol-gel techniques

Jonathan M. Schuster [a,b,c,d,*], María L. Vera [a,b], Carlos E. Schvezov [a], Mario R. Rosenberger [a,b]

[a] Instituto de Materiales de Misiones (IMAM), Universidad Nacional de Misiones (UNaM), Consejo Nacional de Investigaciones Científicas y Técnicas (CONICET), Félix de Azara 1552, C.P. 3300 Posadas, Misiones, Argentina
[b] Universidad Nacional de Misiones (UNaM), Facultad de Ciencias Exactas, Químicas y Naturales (FCEQyN), Programa de Materiales, Modelización y Metrología, Ruta 12, km 7.5, C.P. 3300, Miguel Lanús, Posadas, Misiones, Argentina
[c] Universidad Nacional del Alto Uruguay (UNAU), Departamento de Ciencias de la Salud, Cátedra de Física Biomédica, Avenida Tejeda 1042, C.P. 3364 San Vicente, Misiones, Argentina
[d] Comisión Nacional de Energía Atómica (CNEA), Universidad Nacional de San Martín (UNSAM), Instituto Sabato, Avenida General Paz 1499, C.P. 1650 San Martín, Buenos Aires, Argentina

ARTICLE INFO

Keywords:
Titanium dioxide
Anodic oxidation
Sol-gel process
Rutile
Anatase
Biomedical applications

ABSTRACT

Titanium oxide provides biological and hemocompatible properties to different biomedical devices made of titanium or its alloys. However, since this oxide naturally has a very low thickness and low tribological performance, it would be interesting to obtain thicker and more resistant oxides. In this work, a nanoporous/compact titanium oxide coating was synthesized on the Ti-6Al-4V alloy by combining the anodic oxidation and sol-gel dip-coating techniques. This coating was characterized by optical microscopy, scanning electron microscopy, atomic force microscopy, profilometry and X-ray diffraction. A ~600 nm-thick coating with low roughness (Ra ≅ 50 nm and Sa ≅ 57 nm) and free of cracks was obtained. The coating does not hide the nano- and micro-roughness of the substrate on which it was synthesized. The crystalline structure of the coating is anatase and rutile, but, superficially (~100 nm), it is only anatase.

1. Introduction

Titanium and its alloys are widely used in the manufacture of different medical devices, such as surgical instruments and implantable prostheses, due to their excellent mechanical properties, corrosion resistance, antimagnetic properties, and biocompatibility [1–5]. In particular, the Ti-6Al-4V alloy is widely used for the manufacture of biomedical devices (mechanical heart valve, pacemakers, dental prosthesis, hip prosthesis, etc.) due to its well-known tribological properties, as well as for having a passive layer of titanium oxide (TiO_2) with excellent biocompatibility and hemocompatibility [5–10]. The oxide layer forms naturally on the metal when it is exposed to ambient air; however, it is very thin (1.5–10 nm) and may have cracks that degrade its properties [10,11]. Therefore, to achieve coatings with suitable tribological and biocompatibility properties, it is necessary to use techniques that allow a controlled growth of the thickness of the continuous TiO_2 layer [11–14]. In addition to achieving a greater thickness of the TiO_2 layer, in the case of materials that will be in contact with blood, the coating must be free of cracks and be of low roughness to prevent the formation of clots and adhesion of blood platelets on the surface, and thus improve their hemocompatibility. Also, in the event that the device has moving parts, these characteristics will cause a smoother sliding of the surface and a lower coefficient of friction [15–19].

TiO_2 coatings can be obtained through a wide variety of methods, such as chemical vapor deposition, physical vapor deposition, electrodeposition, electrophoresis, laser ablation, anodization, thermal oxidation of Ti metal, sputtering, cathodic arcs, electrochemical methods, sol-gel, impregnation, ion implantation, etc. Although some of these techniques are expensive and/or very complex [20–22], the sol-gel method and the electrochemical method of anodic oxidation are low-cost and simple and also allow great versatility in terms of the composition, crystallinity, thickness, roughness and nanostructure of the TiO_2 coating obtained [20].

* Corresponding author at: Universidad Nacional de Misiones (UNaM), Facultad de Ciencias Exactas, Químicas y Naturales (FCEQyN), Programa de Materiales, Modelización y Metrología, Ruta 12, km 7.5, C.P. 3300, Miguel Lanús, Posadas, Misiones, Argentina.
E-mail address: jschuster@fceqyn.unam.edu.ar (J.M. Schuster).

https://doi.org/10.1016/j.surfcoat.2022.129035
Received 14 September 2022; Received in revised form 17 October 2022; Accepted 2 November 2022
Available online 9 November 2022

To achieve good tribological behavior, TiO_2 coatings for biomedical applications must have a considerable thickness [23–27]. Although smooth coatings with low roughness and low thickness (<200 nm) can be obtained [2,13,28,29] with various coating synthesis techniques, increasing the thickness of the coating produces an increase in roughness, surface irregularity and even the presence of cracks, resulting in important changes in the micro and nanotopography in relation to the surface of the uncoated titanium alloy [26,30–33]. As mentioned, these changes in roughness and topography can impair the hemocompatibility of the surface, therefore, it is of interest to synthesize smooth TiO_2 coatings with a considerable thickness that maintains or reduces the roughness of the substrate on which they are synthesized.

Thus, to obtain a TiO_2 coating on the Ti-6Al-4V alloy with good tribological and hemocompatibility properties, that is, with a significant thickness, smooth and without cracks, in the present work the anodic oxidation and sol-gel dip-coating techniques were combined. The advantage of the anodic oxidation technique is that it can generate a coating of considerable thickness and great adherence to the substrate, whereas that of sol-gel dip-coating technique is that it can generate smooth and continuous coatings.

2. Experimental methods

2.1. Coating methods and procedures

2.1.1. Preparation of Ti-6Al-4V alloy substrates

From 2-mm-thick titanium alloy grade 5 (Ti-6Al-4V) plates, 20 × 20 mm rectangular samples were prepared by saw cutting. These samples were polished with SiC abrasive papers of decreasing granulometry of #120, #320, #500, #1000 and #1500. Subsequently, the samples were cleaned with water and detergent, then sprayed with alcohol and dried with hot air. These samples, called TI, were used as a substrate to synthesize the different coatings.

2.1.2. Synthesis of nanoporous TiO_2 coatings by anodic oxidation

Anodic oxidation was carried out by circulating a direct current between the Ti-6Al-4V anode, prepared according to Section 2.1.1., and a platinum cathode composed of two strips spaced 5 cm apart and located on opposite sides of the central anode, immersed in a glass container containing a 1 M solution of H_2SO_4 (Cicarrelli, 95–98 %) as electrolyte. A refrigeration system was used to keep the electrolyte temperature below 30 °C. For anodization, a JMB direct current source, model LPS360DD, was used. The oxidation was carried out under spark discharge conditions at a constant voltage of 105 V for 30 s. Under these conditions previous experiments showed that thick nanoporous coatings can be obtained and the use of larger voltages produce dangerous conditions due to development of electrical discharge and temperature increase of the electrolyte [2,34]. The evolution of the voltage and current during the oxidation was recorded. Immediately after oxidation, the samples were removed from the electrolyte and immersed in demineralized water, finally sprayed with alcohol, and dried with hot air. Samples with anodic coating are here called TA.

2.1.3. Synthesis of semicompact TiO_2 coatings by sol-gel dip-coating

For the synthesis of the sol, two solutions were prepared: solution A and solution B. Solution A was prepared by mixing titanium tetrabutoxide (Sigma-Aldrich, ≥97 %) and isopropyl alcohol (Biopack, ≥99.0 %), and stirring for 2 min. After stirring, ethyl acetoacetate (Riedel-de Haën, ≥99.0 %) was added and the mixture was stirred again for 10 min. Stirring was performed using a magnetic stirrer (Arcano-78HW1) at medium speed with the container lid closed. For solution B, isopropyl alcohol, water, and nitric acid (Anedra, 65 %) were mixed in a beaker. This mixture was stirred for 1 min at medium speed. The two solutions were mixed by stirring solution A and adding solution B dropwise. The solution obtained (sol AB) was stirred at medium speed for 1 h with the container lid closed. Then, the AB sol was aged in a refrigerator at 4 °C for 24 h, prior to its use for the production of the coatings. The molar ratios of the reagents used for the synthesis of sol AB are shown in Table 1. The molar concentration of hydrogen ions in the sol was 0.01 M.

Table 1
Molar ratios of the reagents used for the synthesis of the sol.

Reagents	Molar ratio
Ethyl acetoacetate/Titanium tetrabutoxide	0.5
Isopropyl alcohol/Titanium tetrabutoxide	20
Water/Titanium tetrabutoxide	1

Table 2
Volumes used for the synthesis of a sol from 11 mL of titanium tetrabutoxide.

Reagent	Volume [mL]
Titanium tetrabutoxide	11.0
Isopropyl alcohol	49.40
Deionized water	0.58
Ethyl acetoacetate	2.04
Nitric acid	0.044
Total volume	63.1

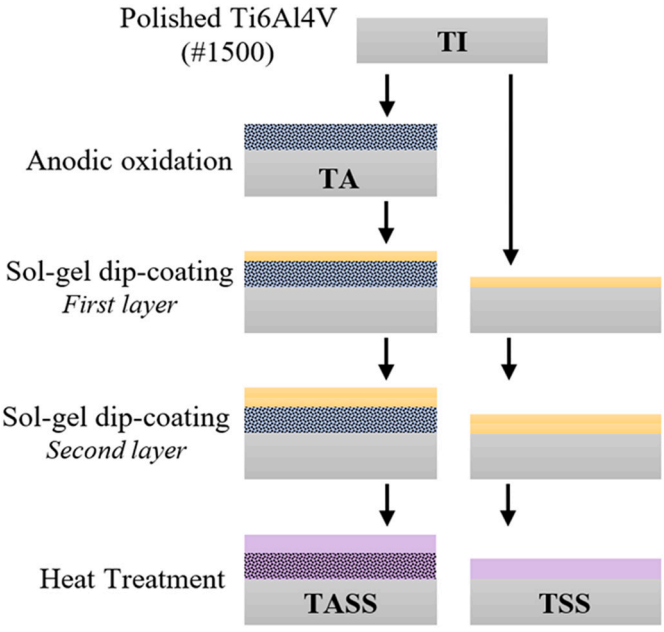

Fig. 1. Scheme of the process to obtain the samples studied in this work: TI, TA, TSS and TASS.

The volume of each reagent used was calculated starting from an arbitrary volume of titanium tetrabutoxide and solving a system of five equations with five unknowns (total volume of the sol, volume of water, volume of ethyl acetoacetate, volume of isopropyl alcohol, and volume of nitric acid). An example of the volumes used for the synthesis of a sol from 11 mL of titanium tetrabutoxide is shown in Table 2.

For the deposition of the sol on the samples, the dip-coating technique, which consists of immersing the substrate in the sol and withdrawing it vertically at a constant speed [35], was used. An extraction speed of 1 mm/s was used. Then, the sample was allowed to dry at room temperature (25 °C) in a normal atmosphere for 20 min (drying I). To complete the drying, the coated samples were placed in a furnace at 150 °C for 15 min (drying II). This completed the deposition of the first sol-gel layer. For the deposition of a new layer, the dip-coating technique was repeated until drying II. In this work, two layers of sol-gel coatings were deposited: one on the TI sample (Ti-6Al-4V), resulting

in the TSS sample, and the other on the titanium oxide layer obtained by anodic oxidation (TA), resulting in the TASS sample.

2.1.4. Heat treatment

The synthesized samples were subjected to a heat treatment in an electric resistance furnace (Simcic) at a temperature of 500 °C for 60 min in an air atmosphere with a heating ramp of 10 °C/min. Cooling was slow, inside the furnace.

2.1.5. Types of samples obtained

Fig. 1 shows a scheme that summarizes the synthesis steps and treatments performed to obtain each of the samples studied in this work: TI (polished Ti-6Al-4V), TA (polished Ti-6Al-4V + anodic oxidation), TSS (polished Ti-6Al-4V + two layers of sol-gel dip-coating + heat treatment) and TASS (polished Ti-6Al-4V + anodic oxidation + two layers of sol-gel dip-coating + heat treatment).

2.2. Characterization of the coatings

2.2.1. Surface characterization

The surface of the samples was observed with a Carl Zeiss Axio Lab. A1 MAT HAL 50 optical microscope and with a Carl Zeiss Supra 40 scanning electron microscope (SEM). The nanoporous surfaces of the TA samples were analyzed in detail by means of the determination of the following morphological parameters of the pores: pore area (A_p), pore perimeter (P_p), pore circularity (Ci_p, defined as $Ci_p = 4\,\pi\,A_p/{P_p}^2$) and equivalent diameter of the pore (D_{eq}, defined as the diameter of a circle with the same perimeter as the pore and calculated as $D_{eq} = P_p/\pi$). These values were calculated from a SEM image whose area was 2.7×107 nm^2 (6000 nm × 4500 nm). The surface covered by pores was determined by analyzing 10 spots of 1000 nm × 1000 nm chosen at random in different SEM images. In addition, by means of optical microscopy, the edge effect on the TSS and TASS samples was analyzed and compared.

2.2.2. Semi-quantitative composition

The semi-quantitative composition of the samples was determined from X-ray energy dispersive spectra (EDS) obtained by an Oxford Instruments INCA X-ACT EDS detector coupled to the Carl Zeiss Supra 40 SEM.

2.2.3. Coating thickness

To determine the thickness of the coatings, a focused ion beam coupled with a SEM (FIB-SEM, FEI Helios NanoLab 650) was used. Previously, a protective layer of platinum (~1 μm thick) was deposited on the sample to reduce the damage caused by the beam. Then, a notch was made with the ion beam, which was then observed with the SEM with an inclination of 52°. The thickness was determined by calculating the arithmetic mean of 15 to 20 measurements.

2.2.4. Crystalline structure

X-ray diffraction analyses to identify the oxide phases present were performed with a SmartLab SE-RIGAKU diffractometer with CuKα wavelength, using an accessory for thin films that allows operating with a grazing beam geometry with an angle of incidence of 1°. The peaks corresponding to anatase, rutile and Ti-6Al-4V were taken from the literature [36,37]. The weight fraction of anatase (f_A) was calculated using the following equation [37–39]:

$$f_A = \frac{1}{1 + k\,(I_R/I_A)}$$

where I_R and I_A are the intensities of the peaks for the rutile (110)-plane ($2\theta = 27.42°$) and the anatase (101)-plane ($2\theta = 25.28°$), respectively.

While k is an empirical dimensionless constant whose value is obtained from the literature, values of k=1.26 [38] and k=2.18 [39] were here used. Intensities were determined by calculating the total area of the corresponding peak. The relative standard uncertainty of f_A is approximately 4 % [38].

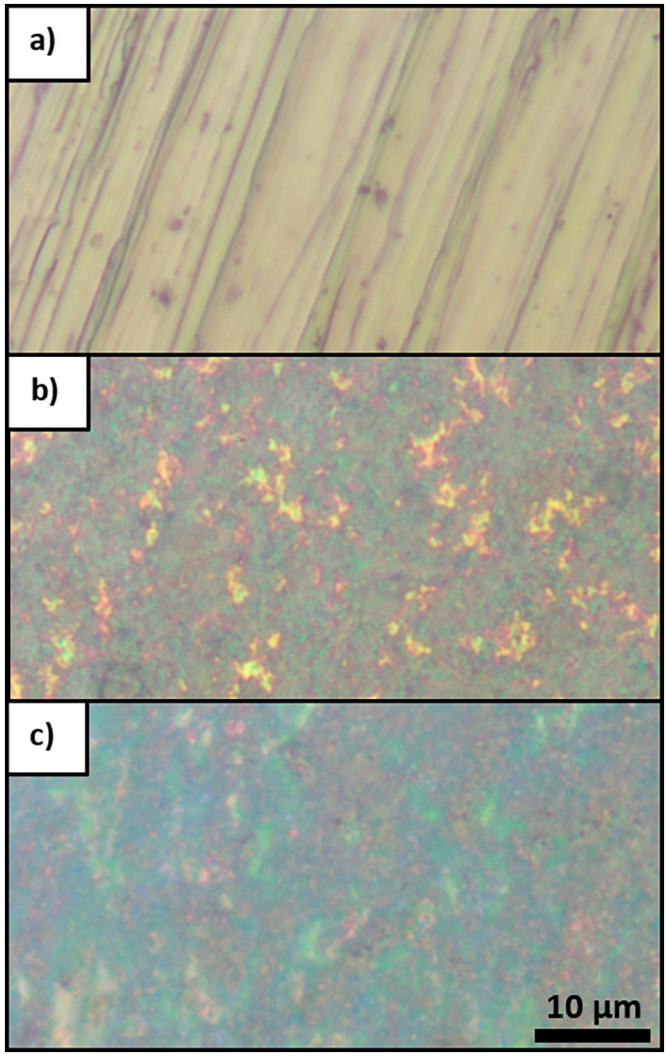

Fig. 2. Images of the surfaces of the TI (a), TA (b) and TASS (c) samples obtained by optical microscopy.

2.2.5. Roughness on the micro- and nanometric scale

To quantify the micro-roughness of the coatings, a Time Group TR-200 roughness meter was used. The following roughness parameters were determined: Ra (arithmetic average height), Rq (root mean square roughness), Rp (maximum height of peaks), Rv (maximum depth of valleys), and Rz (ten-point height). For more details on roughness parameters, see Gadelmawla et al. [40]. In each sample, eight measurements were made in different places, always perpendicular to the polishing lines. A sample length (cut-off) of 0.8 mm and an evaluation length of 0.8 mm were used.

To analyze the topography of the coatings and quantify the nano-roughness, a Bruker Multimode 8 Atomic Force Microscope (AFM) with a Nanoscope V Controller was used. The ScanAsyst method was used to acquire the images, using silicon nitride cantilevers (Scanasyst-Air probes, spring constant = 0.4 N/m, Bruker AFM Probes). The software used to process the images was Gwyddion 2.53. From the images obtained, the roughness parameters Ra, Rq, Rp, Rv and Rz as well as the surface roughness parameters Sa and Sq, which are respectively the extension of Ra and Rq to a surface [41–43], were determined. The sample length (cut-off) in the determinations was L = 1.85 μm, while the projected area of analysis for the roughness spatial parameters (Sa and

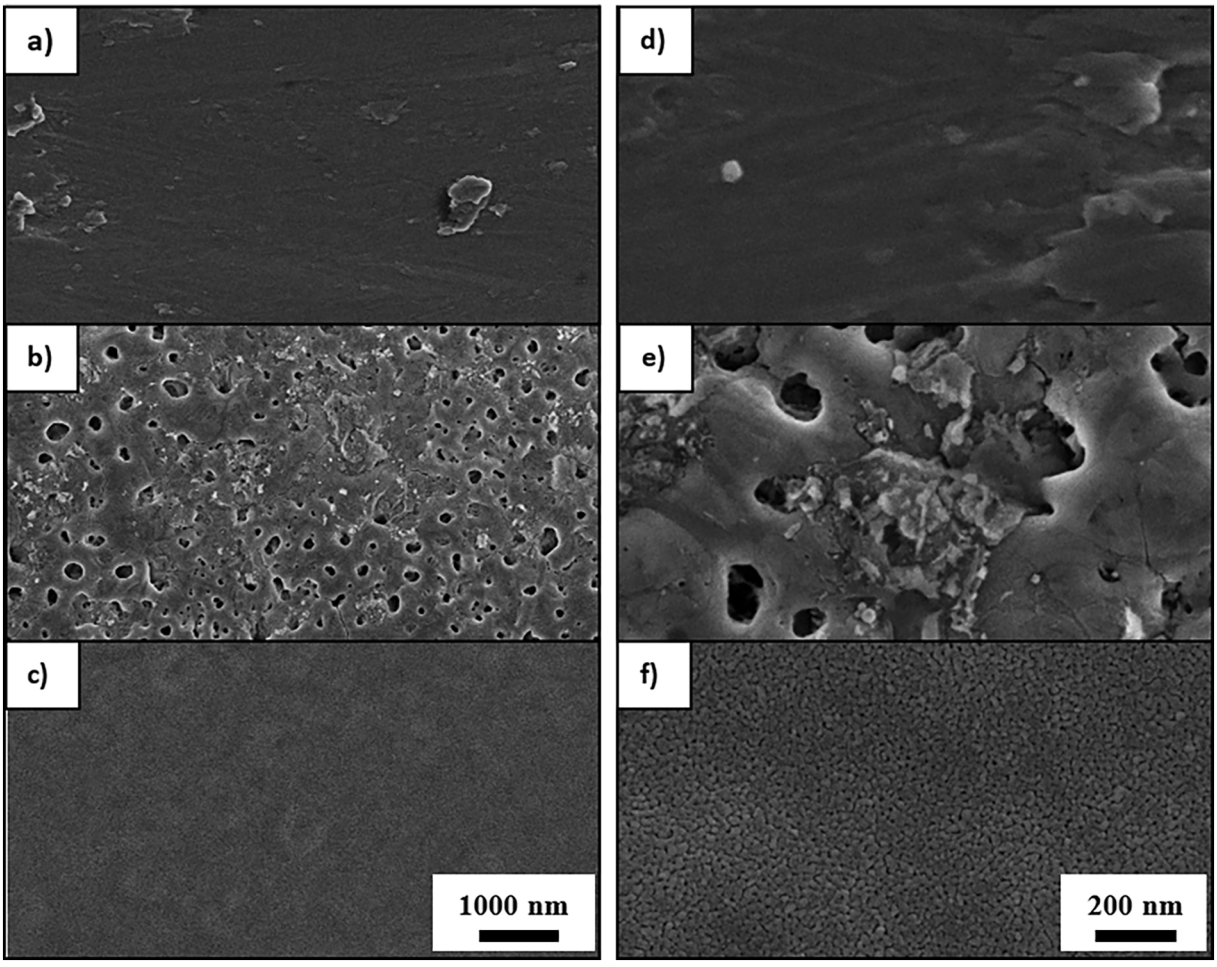

Fig. 3. Images obtained by scanning electron microscopy of the surfaces of the TI (a and d), TA (b and e) and TASS (c and f) samples.

Sq) was 400 μm^2 (20 μm × 20 μm).

2.3. Statistics

The confidence intervals of the morphological parameters of the pores and the roughness parameters at the micro- and nanometric scale were obtained by bootstrap estimation [44]; 95 % confidence intervals were used. The thickness of the coating was analyzed using the Welch ANOVA test (Games Howell Post-hoc Tests). A p-value < 0.05 was considered significant.

3. Results and discussion

3.1. Surface characterization

Surface images of the TI, TA and TASS samples obtained by optical microscopy at different magnifications are shown in Fig. 2.a-c. Fig. 2.a shows the image of a TI sample, in which the scratches that are the product of roughing with #1500 SiC abrasive papers can be clearly observed. Fig. 2.b shows the image of the surface of a TA sample, where a change in the color with respect to the image of the TI sample due to the presence of a TiO_2 nanocoating can be observed [28]. Finally, Fig. 2.c shows the image of a TASS sample, where a change in the color with

Table 3
Estimation and 95 % confidence intervals of the arithmetic mean, median, and 5th and 95th percentiles for the pore area, pore perimeter, pore circularity, and equivalent diameter.

		Area [nm^2]	Perimeter [nm]	Circularity[a] [adim]	Equivalent diameter[b] [nm]
Arithmetic mean	Estimation	7201	279	0.81	89
	CI 95 %	[5346, 9276]	[244, 319]	[0.79, 0.83]	[77, 101]
Median	Estimation	2710	206	0.83	66
	CI 95 %	[1799, 4055]	[172, 251]	[0.80, 0.85]	[55, 79]
5th percentile	Estimation	662	104	0.60	33
	CI 95 %	[510, 855]	[86, 111]	[0.54, 0.66]	[27, 35]
95th percentile	Estimation	32,024	709	0.95	226
	CI 95 %	[23,068, 36,035]	[649, 770]	[0.93, 0.96]	[206, 247]

Confidence intervals obtained by bootstrapping [44].
[a] Circularity = 4 π Area/$Perimeter^2$. A circularity value of 1.0 indicates a perfect circle, whereas a value close to 0.0 indicates an increasingly elongated polygon.
[b] Diameter = Perimeter/π. Diameter of a circle with the same perimeter as the pore.

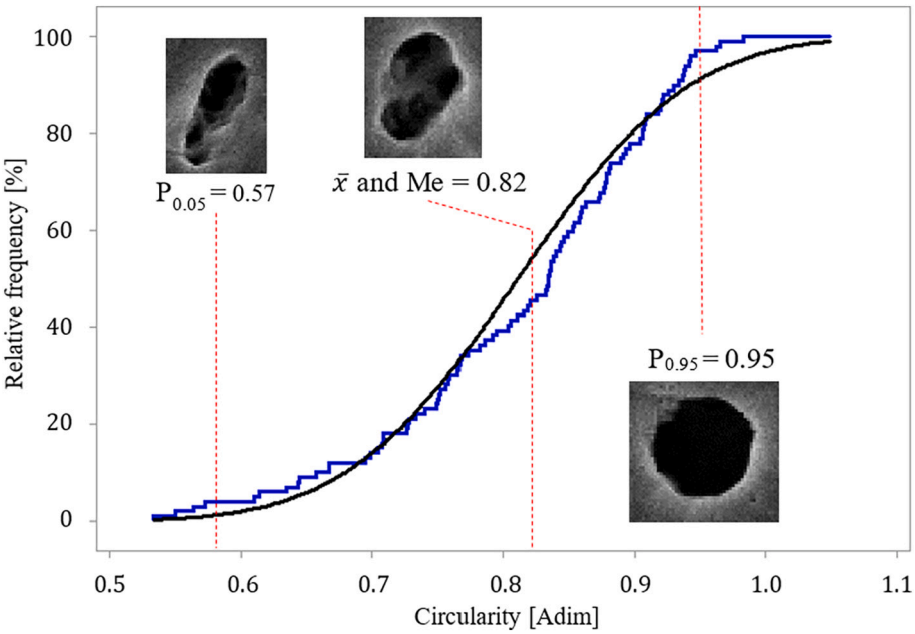

Fig. 4. Empirical distribution of pore circularity values. Representative pores of the arithmetic mean ($\bar{x}$), median (Me), 5th percentile ($P_{0.05}$), and 95th percentile ($P_{0.95}$) are shown. The solid black line shows a fitted normal distribution with the same arithmetic mean and standard deviation as the empirical distribution.

respect to the TA sample due to the fact that the TiO_2 coatings have a different thickness and crystalline structure [45], as described in Sections 3.3 and 3.4, can be observed. The absence of cracks and delamination in the coating on the TASS sample can also be observed.

Fig. 3.a and .d show images of the surface of a TI sample at different magnifications obtained by SEM, in which the characteristic surface of Ti-6Al-4V subjected to abrasion can be observed. This process produces abrasive wear, where fragments of the alloy break off and remain trapped between the abrasive and the surface. This leads to a mechanical mixing, which causes a large amount of plastic deformation of the surface [46,47]. Fig. 3.b and .e show images of a TA sample, in which the presence of a nanoporous coating, which is a product of the evolution of oxygen during the spark discharge process during anodizing [2,12], can be observed. Finally, Fig. 3.c and .f show images of a TASS sample, in which it can be seen that the surface obtained is smooth and free of cracks and also that the TiO_2 coating is composed of nanoparticles (≪50 nm) of TiO_2 whose structure is typical of sol-gel synthesis [48].

3.1.1. Morphological parameters of the nanoporous anodic coating (TA)

The nanoporous coating obtained on the TA samples was analyzed in detail (Fig. 2.b and .e). Table 3 shows the values and statistics of the pore area, its perimeter, the circularity of the pore and its equivalent diameter.

The empirical distribution of the pore area has a large positive asymmetry (Fisher's asymmetry coefficient = 1.96), where 80 % of the values are between 500 nm^2 and 10,000 nm^2, while the remaining 20 % are between 10,000 and 42,000 nm^2. As a consequence of this, the arithmetic mean is ~2.6 times greater than the median. Regarding the distribution of the pore perimeter, it also has a positive asymmetry (Fisher's asymmetry coefficient = 1.32), although to a lesser extent than the pore area, so the arithmetic mean is ~1.3 times greater than the median.

The pore circularity distribution is approximately symmetrical, with a mean value of 0.82. Fig. 4 shows the empirical cumulative distribution of pore circularity. It also shows pore images whose circularity value corresponds to the arithmetic mean value, the 5th percentile and the 95th percentile. These data indicate that, in general, the pores are approximately circular.

The form of the empirical distribution of the equivalent diameter is identical to the form of the perimeter, since, for a given pore, the value of the equivalent diameter is a multiple of the perimeter. Fig. 5 shows the empirical distribution accumulated with a fitted log-normal distribution. The equivalent diameter is useful to analyze the approximate size of the pores considering that they are approximately circular. It can be seen that 90 % of the central values of the equivalent diameter are between 33 nm and 226 nm.

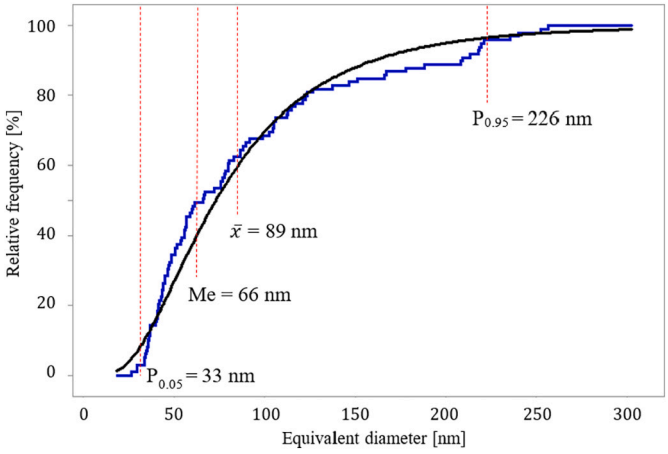

Fig. 5. Empirical distribution of the values of equivalent pore diameter. The values corresponding to the arithmetic mean ($\bar{x}$), median (Me), percentile 5 ($P_{0.05}$) and percentile 95 ($P_{0.95}$) are shown. A solid black line shows a log-normal distribution fitted to the empirical distribution.

The fraction of the surface area covered by pores was 9.9 %, with a confidence interval of 8.3 % to 11.5 %.

3.1.2. Analysis of the edge effect on the TSS and TASS samples

The presence of cracks and delamination at the edges of the TSS and TASS samples was analyzed. The edges are defined according to the position of the sample in the dip-coating process: top, bottom and sides. When the sample is withdrawn from the sol in the dip-coating process, the film deposition process begins. This initial zone is called the upper edge, while the lower zone is the one found at the end of the sample (the

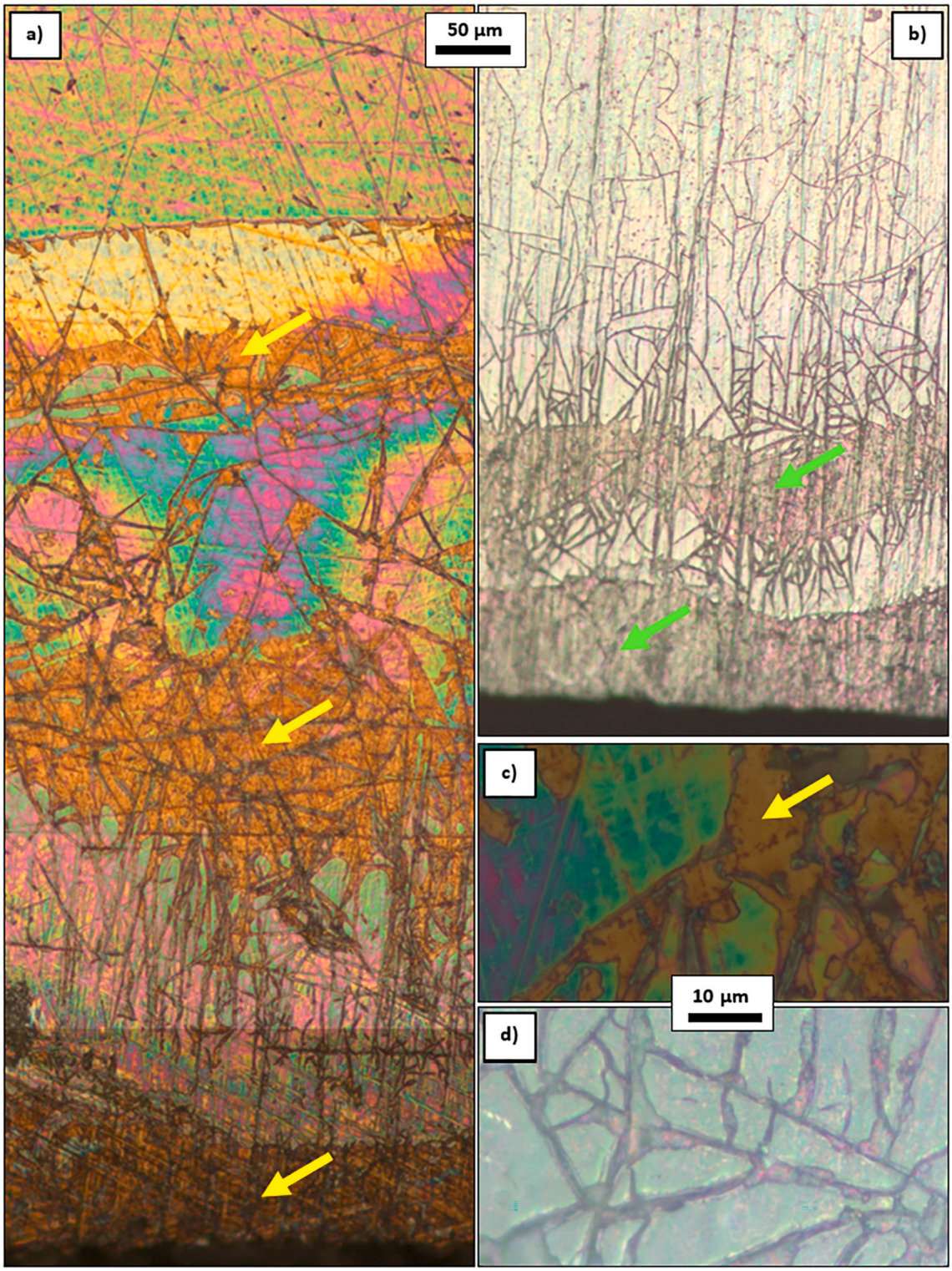

Fig. 6. Representative images of the presence of cracks and delamination on the lower edge of the samples: a) affected area in the TSS sample, b) affected area in the TASS sample, c) detail of the thermal oxide in the TSS sample and d) details of the cracks in the TASS sample. Yellow arrows indicate TI thermal oxide, while green arrows indicate bare TA surface.

last area leaving the sol).

Fig. 6.a shows the lower edge of a TSS sample, in which it can be seen that there is a ca. 1100-µm wide area where the two-layer coating synthesized by sol-gel contains cracks showing zones of the TI substrate with the thermal oxide creating discontinuities in the deposited films. The scratches observed are the product of polishing with SiC abrasive papers of granulometry #1500 (prior to coating). Fig. 6.c shows the absence of the sol-gel coating and the presence of thermal oxide at higher magnification.

Fig. 6.b shows the lower edge of a TASS sample, in which it can be seen that there is a ca. 400-µm wide area where the two-layer coating synthesized by sol-gel contains a large number of cracks, also creating

Table 4
Semi-quantitative composition of the TI, TA and TASS samples determined by EDS.

Sample	Element	Weight [%]	Atomic [%]
TI	Al	6.1	10.3
	Ti	90.4	86.5
	V	3.5	3.2
	O	0.0	0.0
	Total	100.0	100.0
TA	Al	3.7	3.8
	Ti	59.6	34.6
	V	2.0	1.1
	O	34.8	60.5
	Total	100.0	100.0
TASS	Al	3.1	3.1
	Ti	57.9	32.9
	V	2.0	1.1
	O	37.0	62.9
	Total	100.0	100.0

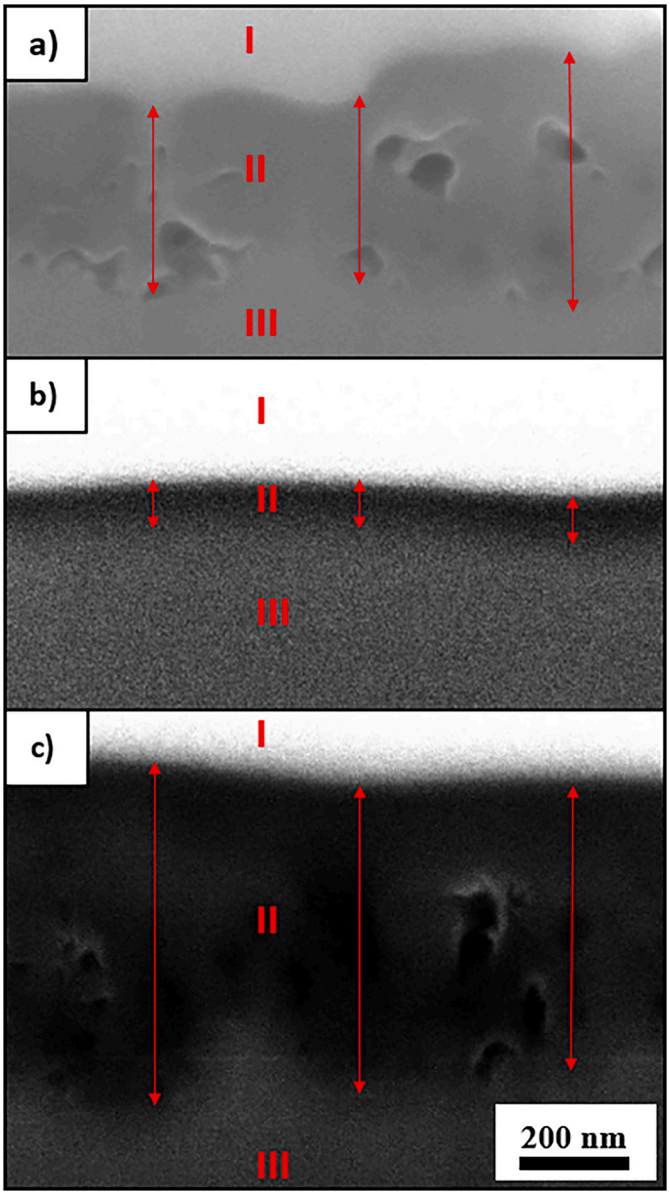

Fig. 7. Cross-sectional images of the TA (a), TSS (b) and TASS (c) samples obtained by focused ion beam microscopy. Ref.: I (platinum protective layer), II (coating), III (Ti-6Al-4V alloy substrate), arrows (local coating thickness).

discontinuities in the deposited films as in the TSS sample, where the TA substrate can be observed. Fig. 6.d shows the cracks at higher magnification.

These results show a reduction of approximately 60 % of the crack and delamination zone, from 1100 μm in the TSS sample to 400 μm in the TASS sample. This reduction may be related to the fact that, in the TASS sample, the coatings are deposited by sol-gel dip-coating on a nanoporous coating (TA) while, in the TSS sample, the coatings are deposited directly on the polished Ti6-Al4-V alloy (TI).

At the upper edge, the affected zone is approximately 100 μm wide in both types of samples (TSS and TASS); however, there are fewer (and

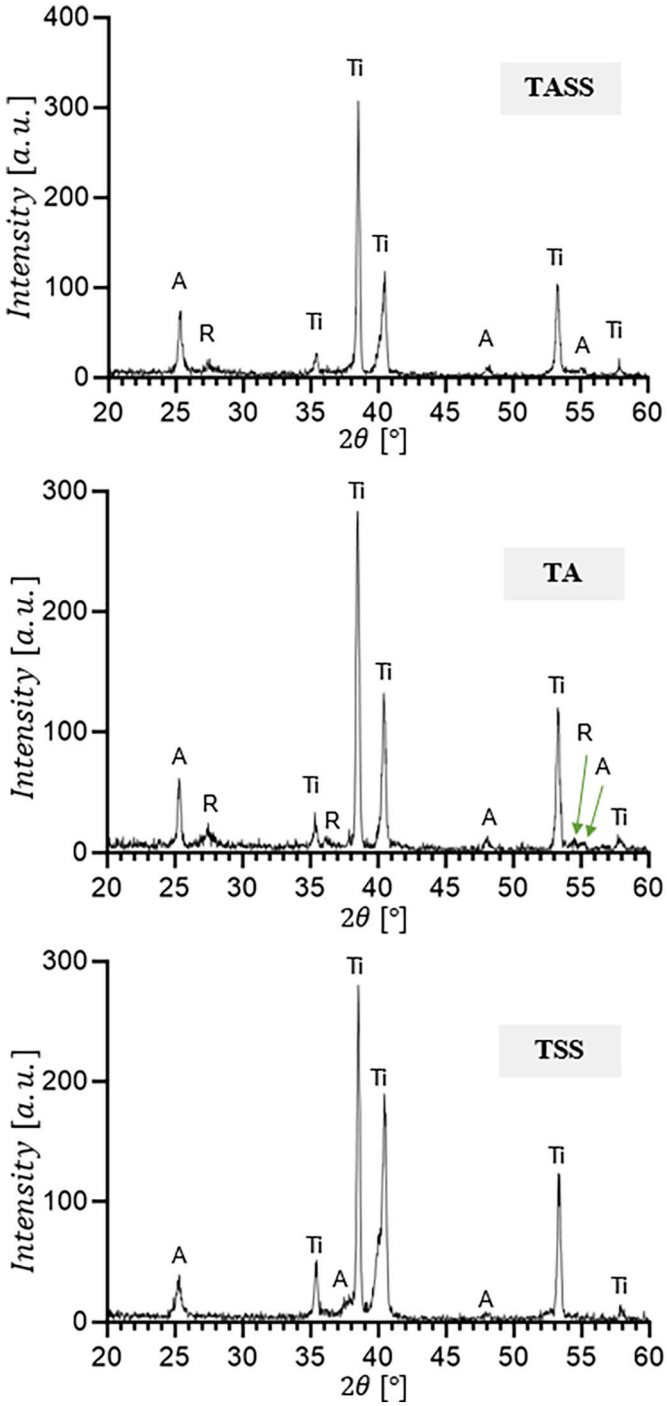

Fig. 8. Diffractograms of TASS, TA and TSS samples. Ref.: A (Anatase), R (Rutile), Ti (Ti-6Al-4V).

smaller) cracks when the sol is deposited on a TA surface than when it is deposited directly on a polished TI surface (polished Ti-6Al-4V alloy).

At the lateral edges, the situation is similar to that described for the lower edge, but, in the case of the sol-gel coating deposited on a TI sample, the affected area is ~800 μm wide, while, in the case of the coating deposited on a TA sample, the affected area is ~500 μm. In other words, the affected area decreases by 37 %.

3.2. Semi-quantitative composition

Table 4 shows the semi-quantitative composition of the TI, TA and TASS samples determined by EDS. In the case of the TI sample, the constituents of the Ti-6Al-4V alloy were detected, but no oxygen was detected despite being covered by a natural native titanium oxide. This result was expected because the thickness of the oxide film is <10 nm. The quantity of oxygen is therefore lower than the detection capacity of the technique used. In the TA sample, in addition to the alloy components, oxygen was detected in 35 % by weight; this can be explained by the presence of titanium oxide produced by anode oxidation. Finally, in the TASS sample, in addition to the alloy components, oxygen was detected in 37 % by weight; this is due to the presence of titanium oxide produced by anodic oxidation and the coating synthesized by sol-gel dip-coating.

3.3. Coating thickness

Fig. 7 shows cross-sectional images of the coatings, where the presence of isolated nanopores (apparently not interconnected) can be observed in the thickness of the TA sample (Fig. 7.a), and in the lower layer of the TASS sample close to the substrate (Fig. 7.c). Fig. 7.b shows the profile of a compact layer, corresponding to the TSS sample, which is also observed in the upper layer of the TASS sample (Fig. 7.c).

Regarding the thickness of the coatings, the arithmetic mean of the measurements in the TA, TSS and TASS samples was 551.6 nm, 89.2 nm and 631.7 nm, respectively, while the standard deviation was 117.6 nm, 11.8 nm and 95.7 nm, respectively. Statistically significant evidence showed that the coatings have thicknesses that are different from each other (p-value = 0.0001). It should be noted that the thickness of the TASS sample (~630 nm) is very similar to the sum of the thicknesses of TA and the TSS (~550 nm + ~90 nm = ~640 nm). In addition, each layer of sol-gel deposited is approximately 45 nm.

In the combined coating, TASS, the sol gel film achieves mechanical integration since the sol partially penetrates the nanoporous structure (as can be seen in the image of Fig. 7.c) where it subsequently crystallizes and sinters during thermal treatment. This could increase the mechanical resistance of these coatings, which is been currently evaluated and will be published.

3.4. Crystalline structure

Fig. 8 shows the diffractograms of the TA, TSS and TASS samples. Regarding the crystalline phases of TiO_2, it can be seen that the TA and TASS samples have anatase and rutile peaks, while the TSS samples have only anatase peaks. Peaks corresponding to the Ti-6Al-4V alloy can be observed in all of them.

The weight fraction of the anatase phase (f_a) found in the TA samples was 0.53 ± 0.02 (using k=1.26) and 0.39 ± 0.02 (using k=2.18), while that in the TASS samples was 0.94 ± 0.02 (using k= 1.26) and 0.90 ± 0.04 (using k=2.18), that is, an increase of 0.41 and 0.51 respectively in the weight fraction of the anatase phase. This increase in the f_a value is due to the fact that the TASS samples result from the combination of TA and two layers of TiO_2 deposited by sol-gel. In the latter two layers, the diffractograms of the TSS samples show that the rutile phase is absent

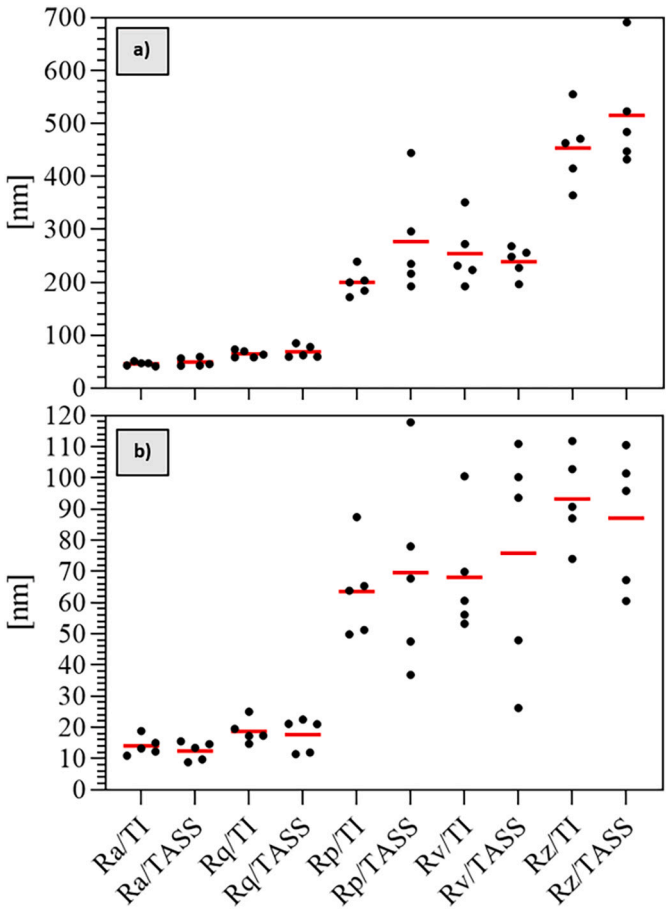

Fig. 9. Roughness parameters determined by profilometry (a) and AFM (b). Ref.: Red line: arithmetic mean.

and that only the anatase phase is present, this is because at normal pressure, the transformation temperature of anatase to rutile is about 600 °C [37], so it is expected that rutile peaks will not be present, since the heat treatment temperature was 500 °C. In the case of the TA and TASS samples, the energy to cause the partial transformation of anatase to rutile comes from the highly energetic conditions of the anodic oxidation process under spark discharge conditions. Therefore, the rutile phase detected in the TASS samples is located in a region far from the surface (approximately 100 nm deep, achieved by the X-rays) and corresponds to the anodic layer. This is important to analyze the surface properties that depend on the crystalline phase present, such as the interaction with biological systems (for example, blood) [4,8,36] because, in the case of TASS samples, the only crystalline phase of TiO_2 that would come into contact with the biological system would be the anatase phase.

3.5. Roughness on the micro- and nanometer scale

Fig. 9.a shows a dot plot with the values of Ra, Rq, Rp, Rv and Rz obtained by profilometry (micro-roughness) in the TI and TASS samples. The red horizontal line shows the arithmetic mean of five measurements. No significant statistical differences were found between the TI and TASS samples between the mean values of any of the roughness parameters (bootstrap estimation, α = 0.05). The mean value for Ra, Rq, Rp, Rv and Rz was ~50 nm, ~70 nm, ~260 nm, ~225 nm and ~485 nm respectively. This shows that the synthesis of the combined coating (anodic oxidation + sol-gel) of the titanium oxide present in the TASS

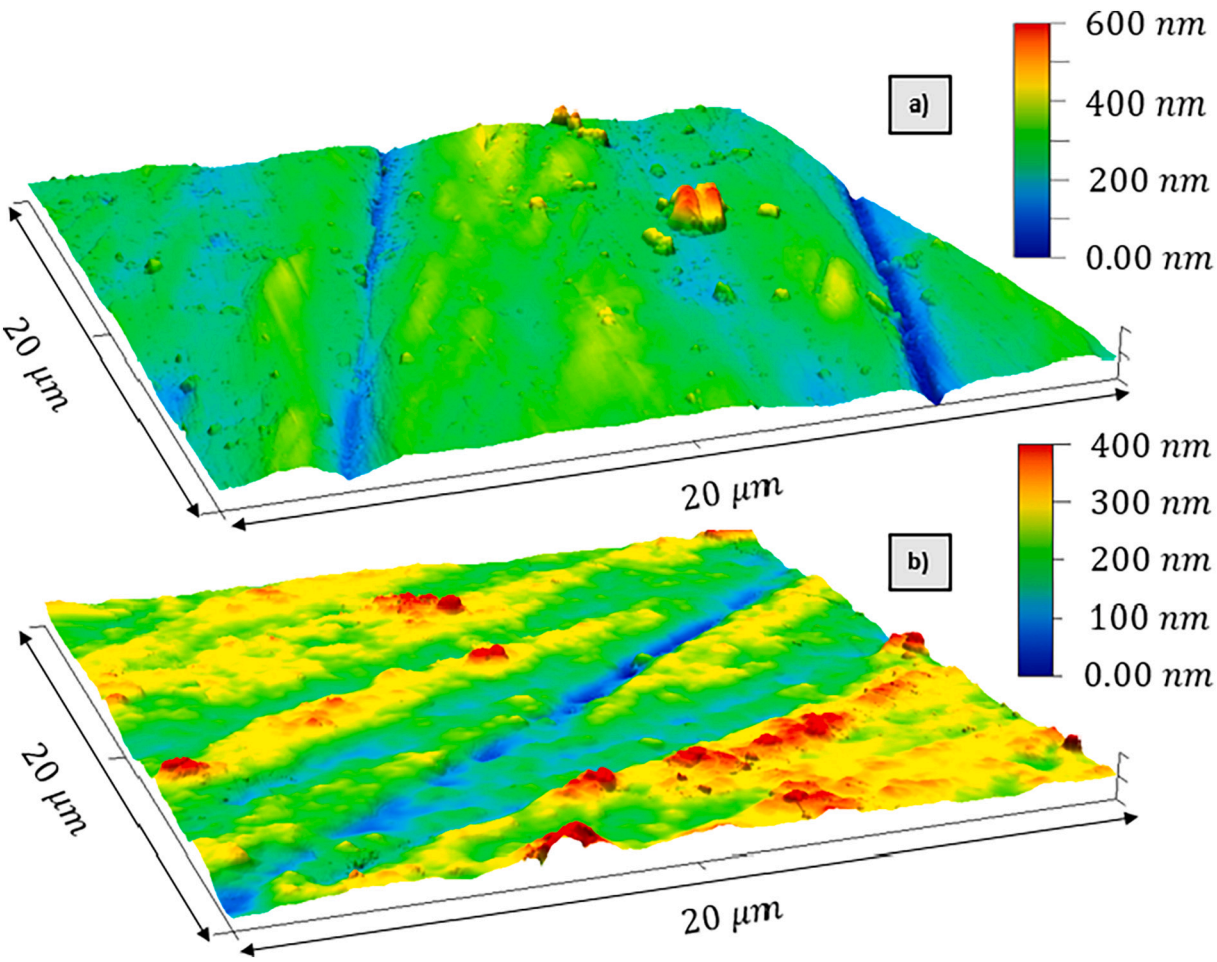

Fig. 10. Three-dimensional views obtained by AFM of the TI (a) and TASS (b) surfaces.

samples does not hide the surface micro-roughness of the substrate (TI). Vera et al. [28] observed the same behavior when synthesizing smooth titanium oxide coatings by means of anodic oxidation (in pre-spark conditions) and thermal oxidation on the Ti-6Al-4V alloy. In that work, the alloy was polished to a mirror level, obtaining a value of Ra equal to 20 nm, and the authors reported that, in general, when synthesizing titanium oxides, the Ra value was maintained and even seemed to increase with the anodizing voltage.

Fig. 9.b shows a dot plot with the values of Ra, Rq, Rp, Rv and Rz obtained by AFM (nano-roughness) in the TI and TASS samples. The red horizontal line shows the arithmetic mean of five measurements. No significant statistical differences were found between the TI and TASS samples between the mean values of any of the roughness parameters (bootstrap estimation, $\alpha = 0.05$). The mean value for Ra, Rq, Rp, Rv and Rz was ~15 nm, ~20 nm, ~65 nm, ~65 nm and ~90 nm respectively. As in the previous case, these data show that the synthesis of the titanium oxide coating present on the TASS samples does not hide the surface nano-roughness of the substrate (TI).

Fig. 10.a and .b show the three-dimensional surface of the TI and TASS samples, respectively. The areas in blue are those corresponding to the polishing scratches and generally have a depth of ~300 nm with respect to the surface that surrounds it. The surface area of the surfaces shown in Fig. 10.a and .b is 409 μm^2 and 407.2 μm^2 respectively. No statistically significant differences were found between the Sq and Sa values of the TI and TASS samples (bootstrap estimation, $\alpha = 0.05$). The average value of Sq is ~61 nm, while that of Sa is ~57 nm.

4. Conclusions

Starting from the Ti-6Al-4V alloy polished up to #1500 and by combining two TiO_2 synthesis techniques, a ~600-nm thick coating with a low roughness (Ra ≅ 50 nm and Sa ≅ 57 nm) was obtained. The coating is made of a nanoporous TiO_2 coating of about 500 nm, synthesized by anodic oxidation, and two layers of smooth TiO_2 nanocoatings of about 50 nm each, synthesized by sol-gel dip-coating. The coating obtained consists of a compact part (near the surface) and a nanoporous part (between the compact part and the substrate). The resulting surface is smooth, with the same roughness as the Ti-6Al-V substrate, and free of cracks and delamination except for a small part close to the edges of the sample.

In addition, a reduction in the extension of the edge effect (cracks and delamination) was observed when TiO_2 sol-gel dip-coating was deposited on the nanoporous surface obtained by anodic oxidation (TA) compared with TiO_2 sol-gel dip-coating deposition directly on the Ti-6Al-4V alloy.

The rutile and anatase crystalline phases are present in the coating; however, only the anatase phase is present in the most superficial portion of the coating.

The coating obtained has great potential for application in biomedical devices where good tribological properties as well as good bio- and hemocompatibility are required.

CRediT authorship contribution statement

Jonathan M. Schuster: Conceptualization, Methodology,

Investigation, Writing – original draft, Writing – review & editing, Visualization. **María L. Vera:** Methodology, Investigation, Writing – review & editing, Funding acquisition. **Carlos E. Schvezov:** Conceptualization, Resources, Writing – review & editing, Supervision. **Mario R. Rosenberger:** Conceptualization, Methodology, Investigation, Resources, Writing – original draft, Writing – review & editing, Supervision, Funding acquisition.

Declaration of competing interest

The authors declare that they have no known competing financial interests or personal relationships that could have appeared to influence the work reported in this paper.

Data availability

Data will be made available on request.

Acknowledgments

To Dr. Hernan Traid for his collaboration in the synthesis by anodic oxidation. To Dr. Leonardo Lizarraga for the AFM measurements at the Centro de Investigaciones en Bionanociencias (CIBION, CONICET). To Eng. Cristian Cegelski for the X-ray diffraction measurements from the Instituto de Materiales de Misiones (IMAM, UNaM-CONICET). To Dr. Gustavo Giménez for the FIB-SEM measurements at the Instituto Nacional de Tecnología Industrial (INTI).

This work was financed with the Scientific and Technological Research Projects PICT-2017-2494 and PICT-2017-2133 granted by the Agencia Nacional de Promoción de la Investigación, el Desarrollo Tecnológico y la Innovación belonging to the Ministerio de Ciencia, Tecnología e Innovación of the Argentine Republic and with the Executing Unit Project PUE-CONICET-2019-574-APN granted by the Consejo Nacional de Investigaciones Científicas y Técnicas (CONICET).

References

[1] M.A. Arenas, C. Pérez-Jorge, A. Conde, E. Matykina, J.M. Hernández-López, R. Pérez-Tanoira, J.J. de Damborenea, E. Gómez-Barrena, J. Esteba, Doped TiO2 anodic layers of enhanced antibacterial properties, Colloids Surf. B Biointerfaces 105 (2013) 106–112, https://doi.org/10.1016/j.colsurfb.2012.12.051.

[2] M.L. Vera, M.Á. Alterach, M.R. Rosenberger, D.G. Lamas, C.E. Schvezov, A.E. Ares, Characterization of TiO2 nanofilms obtained by sol-gel and anodic oxidation, Nanomater.Nanotechnol. 4 (2014) 1–11, https://doi.org/10.5772/58522.

[3] C.E. Schvezov, M.L. Vera, J.M. Schuster, M.R. Rosenberger, Production and characterization of TiO2 nanofilms for hemocompatible and photocatalytic applications, JOM 69 (2017) 2038–2044, https://doi.org/10.1007/s11837-017-2506-4.

[4] W. DeFlorio, K. Crawford, S. Liu, Y. Hua, L. Cisneros-Zevallos, M. Akbulut, Facile, fluorine-free fabrication of bacterial antifouling titanium alloy Ti6Al4V surfaces for surgically implanted devices, Surf. Coat. Technol. 443 (2022), 128580, https://doi.org/10.1016/J.SURFCOAT.2022.128580.

[5] M. Niinomi, Mechanical biocompatibilities of titanium alloys for biomedical applications, J. Mech. Behav. Biomed. Mater. 1 (2008) 30–42, https://doi.org/10.1016/j.jmbbm.2007.07.001.

[6] N. Huang, P. Yang, Y.X. Leng, J.Y. Chen, H. Sun, J. Wang, G.J. Wang, P.D. Ding, T. F. Xi, Y. Leng, Hemocompatibility of titanium oxide films, Biomaterials 24 (2003) 2177–2187, https://doi.org/10.1016/S0142-9612(03)00046-2.

[7] K. Tsuru, S. Hayakawa, A. Osaka, S. Takemoto, T. Yamamoto, S. Takashima, Platelet adhesion on titanium oxide gels: effect of surface oxidation, Biomaterials 25 (2003) 3485–3492, https://doi.org/10.1016/j.biomaterials.2003.10.070.

[8] Y. Kousar, N. Ali, V.F. Neto, S. Mei, J. Gracio, Deposition of nanocrystalline diamond and titanium oxide coatings onto pyrolytic carbon using CVD and sol-gel techniques, Diam. Relat. Mater. 13 (2004) 638–642, https://doi.org/10.1016/j.diamond.2004.01.034.

[9] E. Eisenbarth, D. Velten, K. Schenk-Meuser, P. Linez, V. Biehl, H. Duschner, J. Breme, H. Hildebrand, Interactions between cells and titanium surfaces, Biomol. Eng. 19 (2002) 243–249, https://doi.org/10.1016/S1389-0344(02)00032-1.

[10] V.K. Manivasagam, R.M. Sabino, P. Kantam, K.C. Popat, Surface modification strategies to improve titanium hemocompatibility: a comprehensive review, Mater. Adv. 2 (2021) 5824–5842, https://doi.org/10.1039/D1MA00367D.

[11] J.C.M. Souza, M.B. Sordi, M. Kanazawa, S. Ravindran, B. Henriques, F.S. Silva, C. Aparicio, L.F. Cooper, Nano-scale modification of titanium implant surfaces to enhance osseointegration, Acta Biomater. 94 (2019) 112–131, https://doi.org/10.1016/J.ACTBIO.2019.05.045.

[12] M.L. Vera, J. Schuster, M.R. Rosenberger, H. Bernard, C.E. Schvezov, A.E. Ares, Evaluation of the haemocompatibility of TiO2 coatings obtained by anodic oxidation of Ti-6Al-4V, ProcediaMater. Sci. 8 (2015) 366–374, https://doi.org/10.1016/j.mspro.2015.04.086.

[13] M.L. Vera, M.R. Rosenberger, C.E. Schvezov, A.E. Ares, Wear resistance of anodic titanium dioxide films produced on Ti-6Al-4V alloy, Nanomater.Nanotechnol. 5 (2015) 1–7, https://doi.org/10.5772/60069.

[14] X. Jin, L. Gao, E. Liu, F. Yu, X. Shu, H. Wang, Microstructure, corrosion and tribological and antibacterial properties of Ti-Cu coated stainless steel, J. Mech. Behav. Biomed. Mater. 50 (2015) 23–32, https://doi.org/10.1016/j.jmbbm.2015.06.004.

[15] J.F. Hecker, L.A. Scandrett, Roughness and thrombogenicity of the outer surfaces of intravascular catheters, J. Biomed. Mater. Res. 19 (1985) 381–395, https://doi.org/10.1002/JBM.820190404.

[16] J. Lu, C. Yao, L. Yang, T.J. Webster, in: Decreased Platelet Adhesion and Enhanced Endothelial Cell Functions on Nano and Submicron-Rough Titanium Stents 18, 2012, pp. 1389–1398, https://doi.org/10.1089/TEN.TEA.2011.0268. https://home.liebertpub.com/tea.

[17] S. Karthikeyan, B. Mohan, S. Kathiresan, G. Anbuchezhiyan, Effect of process parameters on machinability, hemocompatibility and surface integrity of SS 316L using R-MRAFF, J.Mater.Res.Technol. 15 (2021) 2658–2672, https://doi.org/10.1016/J.JMRT.2021.09.060.

[18] T. Hasebe, T. Ishimaru, A. Kamijo, Y. Yoshimoto, T. Yoshimura, S. Yohena, H. Kodama, A. Hotta, K. Takahashi, T. Suzuki, Effects of surface roughness on antithrombogenicity of diamond-like carbon films, Diam. Relat. Mater. 16 (2007) 1343–1348, https://doi.org/10.1016/j.diamond.2006.12.009.

[19] G. Tepe, J. Schmehl, H.P. Wendel, S. Schaffner, S. Heller, M. Gianotti, C. D. Claussen, S.H. Duda, Reduced thrombogenicity of nitinol stents—in vitro evaluation of different surface modifications and coatings, Biomaterials 27 (2006) 643–650, https://doi.org/10.1016/J.BIOMATERIALS.2005.06.004.

[20] M.I. Litter, M.L. Vera, H.D. Traid, TiO2 coatings prepared by sol-gel and electrochemical methodologies, in: Sol-Gel Derived Optical and Photonic Materials, 2020, pp. 39–74, https://doi.org/10.1016/B978-0-12-818019-8.00003-X.

[21] G. Wang, J. Li, K. Lv, W. Zhang, X. Ding, G. Yang, X. Liu, X. Jiang, Surface thermal oxidation on titanium implants to enhance osteogenic activity and in vivo osseointegration, Sci. Rep. 6 (2016), https://doi.org/10.1038/srep31769.

[22] M. Winnicki, L. Łatka, M. Jasiorski, A. Baszczuk, Mechanical properties of TiO2 coatings deposited by low pressure cold spraying, Surf. Coat. Technol. 405 (2021), 126516, https://doi.org/10.1016/J.SURFCOAT.2020.126516.

[23] Y. Sun, Tribological rutile-TiO2 coating on aluminium alloy, Appl. Surf. Sci. 233 (2004) 328–335, https://doi.org/10.1016/J.APSUSC.2004.03.241.

[24] D.Siva Rama Krishna, Y.L. Brama, Y. Sun, Thick rutile layer on titanium for tribological applications, Tribol. Int. 40 (2007) 329–334, https://doi.org/10.1016/J.TRIBOINT.2005.08.004.

[25] Y.X. Leng, J.Y. Chen, P. Yang, H. Sun, N. Huang, Structure and properties of passivating titanium oxide films fabricated by DC plasma oxidation, Surf. Coat. Technol. 166 (2003) 176–182, https://doi.org/10.1016/S0257-8972(02)00780-6.

[26] O. Çomakli, T. Yetim, A. Çelik, The effect of calcination temperatures on wear properties of TiO2coated CP-Ti, Surf. Coat. Technol. 246 (2014) 34–39, https://doi.org/10.1016/j.surfcoat.2014.02.059.

[27] C.E. Schvezov, M.L. Vera, J.M. Schuster, M.R. Rosenberger, Production and characterization of TiO2 nanofilms for hemocompatible and photocatalytic applications, JOM 69 (2017) 2038–2044, https://doi.org/10.1007/s11837-017-2506-4.

[28] M.L. Vera, M.R. Rosenberger, C.E. Schvezov, A.E. Ares, Fabrication of TiO 2 crystalline coatings by combining Ti-6Al-4V anodic oxidation and heat treatments, Int. J. Biomater. 2015 (2015) 1–9, https://doi.org/10.1155/2015/395657.

[29] C.E. Schvezov, M.A. Alterach, M.L. Vera, M.R. Rosenberger, A.E. Ares, Characteristics of hemocompatible TiO2 nano-films produced by the sol-gel and anodic oxidation techniques, JOM 62 (2010) 84–87, https://doi.org/10.1007/s11837-010-0094-7.

[30] A. Çelik, M.T. Acar, T. Yetim, H. Kovacı, A.F. Yetim, Improving structural, tribological and electrochemical properties of Ti6Al4V alloy with B-doped TiO2 thin films, Tribol. Int. 146 (2020), 106210, https://doi.org/10.1016/j.triboint.2020.106210.

[31] M.T. Acar, H. Kovacı, A. Çelik, Enhancement of the tribological performance and surface wettability of Ti6Al4V biomedical alloy with boric/sulfuric acid anodic film, Surf. Topogr. 9 (2021), 035024, https://doi.org/10.1088/2051-672x/ac1d87.

[32] M.S.P. Sarah, M.Z. Musa, M.N. Asiah, M. Rusop, Electrical conductivity characteristics of TiO2 thin film, in: 2010 International Conference on Electronic Devices, Systems and Applications, ICEDSA 2010 - Proceedings, 2010, pp. 361–364, https://doi.org/10.1109/ICEDSA.2010.5503040.

[33] M.K. Ibrahim, M. Kaba, F. Muhaffel, D. Ağaoğulları, H. Cimenoglu, Thermal oxidation of a porous Ti[sbnd]23Nb alloy for wear related biomedical applications: effect of oxidation duration, Surf. Coat. Technol. 439 (2022), https://doi.org/10.1016/j.surfcoat.2022.128429.

[34] H.D. Traid, M.L. Vera, A.E. Ares, M.I. Litter, Advances on the synthesis of porous TiO2 coatings by anodic spark oxidation. Photocatalytic reduction of Cr(VI), Mater. Chem. Phys. 191 (2017) 106–113, https://doi.org/10.1016/J.MATCHEMPHYS.2017.01.034.

[35] C.J. Brinker, G.C. Frye, A.J. Hurd, C.S. Ashley, Fundamentals of sol-gel dip coating, Thin Solid Films 201 (1991) 97–108, https://doi.org/10.1016/0040-6090(91)90158-T.

[36] S.L.R. da Silva, L.O. Kerber, L. Amaral, C.A. dos Santos, X-ray diffraction measurements of plasma-nitrided Ti-6Al-4V, Surf. Coat. Technol. 116–119 (1999) 342–346, https://doi.org/10.1016/S0257-8972(99)00204-2.
[37] D.A.H. Hanaor, C.C. Sorrell, Review of the anatase to rutile phase transformation, J. Mater. Sci. 46 (2011) 855–874, https://doi.org/10.1007/s10853-010-5113-0.
[38] R.A. Spurr, H. Myers, Quantitative analysis of anatase-rutile mixtures with an X-ray diffractometer, Anal. Chem. 29 (1957) 760–762.
[39] J. Criado, C. Real, Mechanism of the inhibiting effect of phosphate on the anatase → rutile transformation induced by thermal and mechanical treatment of TiO2, J. Chem. Soc. Faraday Trans. 1 Phys. Chem. Condens. Phases 79 (1983) 2765–2771, https://doi.org/10.1039/F19837902765.
[40] E.S. Gadelmawla, M.M. Koura, T.M.A. Maksoud, I.M. Elewa, H.H. Soliman, Roughness parameters, J. Mater. Process. Technol. 123 (2002) 133–145.
[41] One-Dimensional Roughness Parameters, (n.d.). http://gwyddion.net/documentation/user-guide-en/roughness-iso.html (accessed March 11, 2019).
[42] R. Deltombe, K.J. Kubiak, M. Bigerelle, How to select the most relevant 3D roughness parameters of a surface, Scanning 36 (2014) 150–160, https://doi.org/10.1002/sca.21113.
[43] P. Pawlus, R. Reizer, M. Wieczorowski, Functional importance of surface texture parameters, Materials 14 (2021), https://doi.org/10.3390/ma14185326.
[44] J.T. DiCiccio, B. Efron, Bootstrap confidence intervals, <sb:contribution><sb:title>Stat. </sb:title></sb:contribution><sb:host><sb:issue><sb:series><sb:title>Sci.</sb:title></sb:series></sb:issue></sb:host> 11 (1996) 181–188, https://doi.org/10.1007/978-3-319-01931-4_24.
[45] M.A. Alterach, P.C. Favilla, M.R. Rosenberger, D.G. Lamas, A.E. Ares, C. E. Schvezov, Resistencia al desgaste de recubrimientos delgados de TiO2 para protesis cardiacas, An.AFA 20 (2008) 147–153.
[46] D.I. Adebiyi, A.P.I. Popoola, Mitigation of abrasive wear damage of Ti-6Al-4V by laser surface alloying, Mater. Des. 74 (2015) 67–75, https://doi.org/10.1016/j.matdes.2015.02.010.
[47] A. Dorner, C. Schürer, G. Reisel, G. Irmer, O. Seidel, E. Müller, Diamond-like carbon-coated Ti6A14V: influence of the coating thickness on the structure and the abrasive wear resistance, Wear 249 (2001) 489–497, https://doi.org/10.1016/S0043-1648(01)00587-7.
[48] V.J. Nagpal, R.M. Davis, S.B. Desu, Novel thin films of titanium dioxide particles synthesized by a sol-gel process, J. Mater. Res. 10 (1995) 3068–3078. http://journals.cambridge.org.